Pergamon

Int. J. Heat Mass Transfer. Vol. 38, No. 4, pp. 643–654, 1995

0017-9310/95 $9.50+0.00

0017-9310(94)00194-4

Effects of heater length and orientation on the trigger mechanism for near-saturated flow boiling critical heat flux—II. Critical heat flux model

CHRISTOPHER O. GERSEY and ISSAM MUDAWAR†

Boiling and Two-Phase Flow Laboratory, School of Mechanical Engineering, Purdue University, West Lafayette, IN 47907, U.S.A.

(*Received* 13 *December* 1993 *and in final form* 17 *June* 1994)

Abstract—A critical heat flux (CHF) model is presented that accounts for both heater length and orientation effects. The model is verified with FC-72 data obtained for 10-, 30- and 110-mm long heaters that were flush-mounted in a 10-mm × 5-mm channel and orientations including vertical upflow, 45-degree inclined flow, and horizontal flow, with liquid flowing above the heaters. The inlet liquid velocity was varied between 25 and 200 cm s^{-1} while maintaining the inlet temperature constant at 4°C subcooling. CHF was found to decrease with heater length but showed little sensitivity to orientation. Formulation of the model was based on flow visualization and photomicrography of the vapor–liquid interface along the heaters. Just prior to CHF, a wavy vapor layer engulfed the heater, allowing liquid access only through wetting fronts where wave troughs touched the heater surface. The distance between wetting fronts increased in the stream-wise direction, decreasing the number of wetting fronts available for liquid replenishment. Lifting of the most upstream wetting front was found to catastrophically cause CHF. The CHF model incorporates the observed stream-wise reduction in wetting fronts with a criterion for lift-off heat flux to obtain a simplified set of equations for CHF. Local information such as pressure, phase velocities, and average vapor layer thickness along the heater were also incorporated in the CHF model using the assumption of separated two-phase flow. The model predicts the CHF data for the 0°, 45° and 90° orientations with mean absolute errors of 12.6, 13.6 and 17.5%, respectively.

INTRODUCTION

Predicting critical heat flux (CHF) has been the focus of a considerable body of research spanning the past three decades. Several researchers have written review articles critically analyzing the many CHF correlations and semi-empirical models [1–4]. Table 1 outlines the six main types of models that encompass virtually all of the CHF research.

The literature also contains many correlations that predict CHF based on geometrical parameters and thermophysical properties. Correlations of this type are generally system dependent and, thus, are useful only in similar situations. Extension of existing correlations to new fluids and geometries often requires the collection of new data bases; empirical constants are then modified to better fit the correlation to the data.

In an attempt to create a more universal model, researchers have refocused their efforts on ascertaining the physical mechanisms responsible for initiating CHF. The bubble crowding and sublayer dryout models attempt to relate some of the near-wall observations of the liquid and vapor to a physical process or trigger mechanism, but the models still rely on empirical constants in order to provide closure. In his review of the status of boiling heat transfer research, Lienhard [25] found the literature to still be lacking a direct experimental observation for the instability that causes CHF in flow boiling.

Recently Galloway and Mudawar [22] used photomicrographic and high speed video imaging techniques to clearly capture this instability. Figure 1(a) illustrates the near-wall liquid and vapor conditions observed by Galloway and Mudawar on a small, 1.6-mm × 12.7-mm heater in vertical upflow of FC-87. Bubbles emanating from the heater surface were observed to coalesce into a vapor wave at heat fluxes below CHF (CHF−). Liquid remained in contact with the heated surface at the most upstream portion of the heater and at the wave troughs. Even though much of the surface beneath the vapor wave was dry, these troughs, referred to as wetting fronts, were able to dissipate the imposed heat flux at CHF−. Figure 1(b) illustrates how CHF occurred after a slight increase in heat flux (CHF+) when the intense vapor production at the heater surface forced the most upstream depression in vapor–liquid interface, corresponding to the most upstream wetting front at CHF−, away from the heated surface. The heat flux in the remaining wetting fronts, in turn, increased and, without the creation of new wetting fronts, the intense boiling also lifted the remaining wetting fronts away from the surface. Without any liquid contact with the

†Author to whom correspondence should be addressed.

NOMENCLATURE

b	fraction of wavelength occupied by the wetting front for waves with $\lambda = 2\lambda_c$
c	interfacial velocity
c_{pf}	specific heat of liquid
CHF	critical heat flux, q''_m
CHF−	heat flux just below q''_m
CHF+	heat flux just above q''_m
D_h	full channel hydraulic diameter, $2wH/(w+H)$
$D_{h,f}$	liquid phase hydraulic diameter, $2w(H-\delta)/(w+H-\delta)$
$D_{h,g}$	vapor phase hydraulic diameter, $2w\delta/(w+\delta)$
f	friction factor
g_n	gravitational acceleration normal to heater surface
g_t	gravitational acceleration tangential to heater surface
h_{fg}	latent heat of vaporization
H	channel height, 5 mm
H_f	average height of liquid layer
H_g	average height of vapor layer
k	wave number, $2\pi/\lambda$
L	heater length in flow direction (10, 30 or 110 mm)
L_1	span of heater corresponding to upstream doubling of wavelengths
L_2	span of heater where λ increases because of wave stretching and merging
L_3	span of heater where λ is constant
N	number of waves touching the heater surface
P	pressure
ΔP	pressure drop
q''	average wall heat flux
q''_m	critical heat flux
t	time
T	temperature
ΔT_{sub}	inlet subcooling, $T_{sat} - T_{f,in}$
U	mean liquid inlet velocity
U_f	mean liquid velocity
U_g	mean vapor velocity
ΔU	$U_g - U_f$
w	channel width, 10 mm
x	thermodynamic equilibrium quality
z	stream-wise coordinate
z_0	upstream region where $\Delta U = 0$
z^*	$z_0 + \lambda_c(z^*)$.

Greek symbols

δ	time-averaged vapor layer thickness
η	displacement of vapor–liquid interface
η_0	amplitude of interfacial wave
λ	wavelength
λ_c	critical wavelength
μ	dynamic viscosity
ρ	density
ρ''_k	$\rho_k \coth(kH_k)$, where subscript k corresponds to liquid or vapor phase
σ	surface tension
τ	shear stress
θ	orientation angle measured from the vertical position.

Subscripts

A	accelerational
f	liquid
F	frictional
g	vapor
G	gravitational
i	interface, imaginary component
in	inlet
k	phase k
meas	measured
r	real component
sat	saturated.

Table 1. Classification of critical heat flux (CHF) models

Model	CHF trigger mechanism	Authors
Boundary layer separation	Intense boiling causes liquid boundary layer separation	Kutateladze and Leont'ev [5]; Tong [6,7]
Mechanical energy criteria	Kinetic energy of vapor exceeds the surface energy of expanding vapor	Lienhard and Eichhorn [8]; Lienhard and Hasan [9]
Bubble crowding	Numerous bubbles on wall inhibit liquid replenishment	Kirby *et al.* [10]; Hebel *et al.* [11]; Weisman and Pei [12]
Sublayer dryout	A liquid layer between a large bubble and the wall dries out momentarily causing a rise in the wall temperature	Fiori and Bergles [13]; Van der Molen and Galjee [14]; Haramura and Katto [15]; Hino and Ueda [16]; Mudawar *et al.* [17]; Lee and Mudawar [18]; Mudawar and Maddox [19]; Katto [20,21]
Interfacial liftoff	Wavy vapor layer engulfs wall except for wetting fronts at the wave troughs; CHF follows lifting of the wetting fronts	Galloway and Mudawar [22–24]

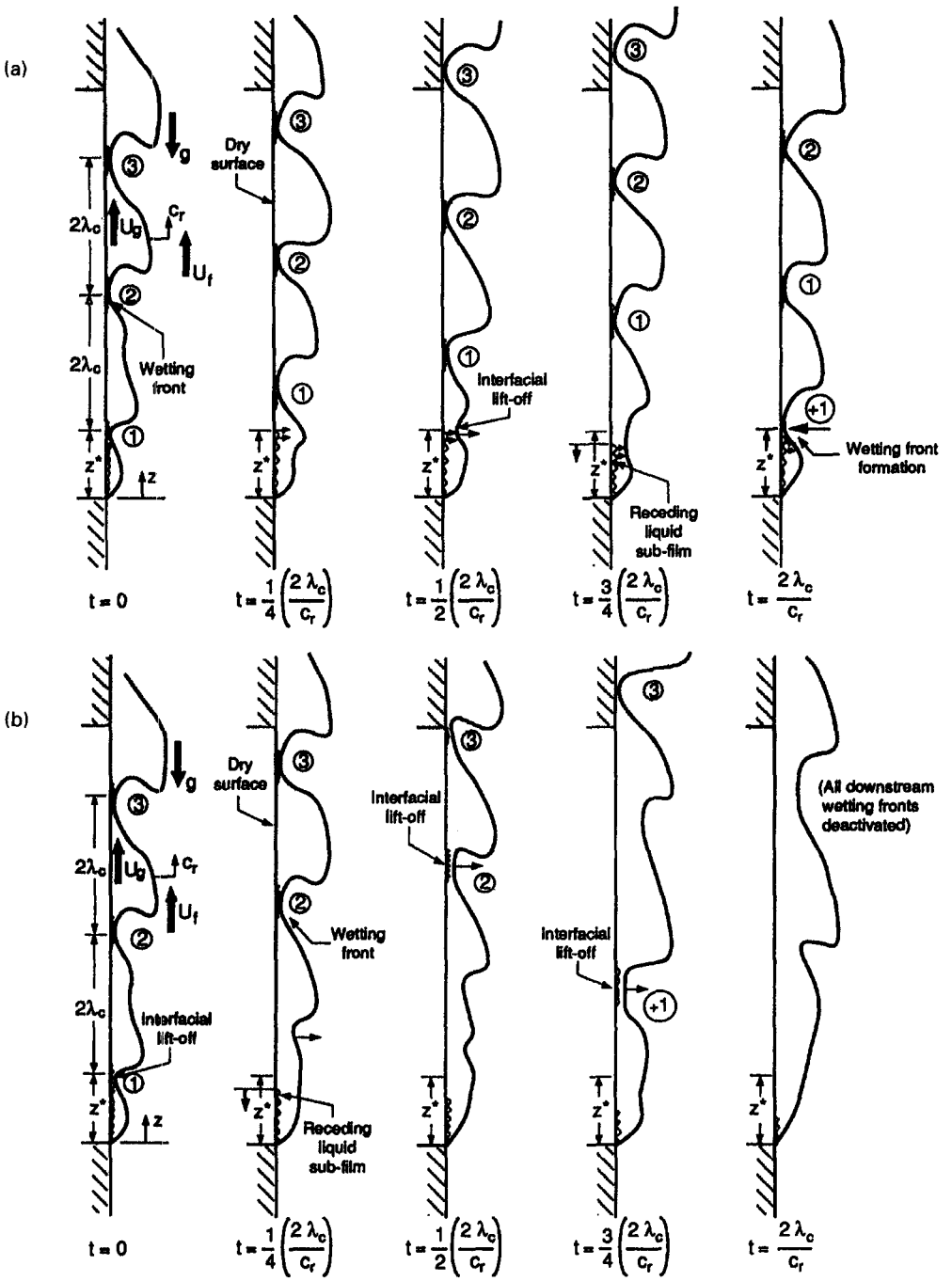

Fig. 1. Illustration of a complete cycle of events observed at (a) CHF− and (b) following a slight increase in heat flux (adapted from Galloway and Mudawar [23]).

surface, the heat transfer coefficient decreased sharply, causing a large and rapid escalation in the heater temperature.

To compute CHF, Galloway and Mudawar [23] calculated a surface energy balance accounting for boiling on a small upstream region ($0 < z < z^*$) of continuous wetting. Wavelengths two-thirds down the heater at CHF− measured twice the critical Kelvin–Helmholtz wavelength based on hydrodynamic conditions at z^*. The number of wetting fronts on the heated surface was

$$N = \mathrm{INT}\left(\frac{L - z^*}{2\lambda_c}\right) + 1 \tag{1}$$

where INT is the integer function. The distance z^* was set equal to $[\lambda_c(z^*) + z_0]$, where z_0 is the point at which the vapor velocity just exceeds the liquid velocity

(where ΔU becomes positive); z_0 is about 0.1 mm for $U = 25$ cm s^{-1}, increasing to 1.0 mm for $U = 200$ cm s^{-1}. In other words, wetting fronts form when the distance from z_0 equals the local critical wavelength calculated from an instability model.

For all of the flow conditions investigated by Galloway and Mudawar, the surface energy balance for the heater yielded the following expression for CHF:

$$q''_m = \left(1 - \frac{b\lambda_c}{4(L-z^*)}\right) bq''_l \tag{2}$$

where $b = 0.25$, the fraction of $2\lambda_c$ occupied by the wetting front, and q''_l is the heat flux required to cause lifting of the wetting front. Lift off was assumed to occur when the normal momentum of vapor produced in the wetting front just exceeded the pressure force exerted on the interface as a result of interfacial curvature:

$$\rho_g \left[\frac{q''_l}{\rho_g h_{fg}\left(1 + \frac{c_{pf}\Delta T_{sub}}{h_{fg}}\right)}\right]^2 = \overline{P_f - P_g}. \tag{3}$$

The average interfacial pressure, $(\overline{P_f - P_g})$, was calculated by integrating the pressure over the span of the most upstream wetting front.

In the first part of this study, wave growth and the lift off criteria were investigated for long heaters in a rectangular channel [26]. Three heater lengths were tested in vertical upflow, inclined flow, and horizontal flow. Vapor waves were observed to grow along the heater as a result of wave stretching and drag-induced wave merging to an asymptotic value of $4\lambda_c$. The CHF trigger mechanism was identified to be lifting of the most upstream wetting front as proposed by Galloway and Mudawar for short heaters.

In this paper, the physical mechanisms causing wave merging are explored and their consequences on CHF for long heaters quantified. The original Galloway and Mudawar lift-off model will be modified to compensate for the stream-wise growth in vapor wavelength. The revised model will be verified by comparing its predictions to CHF data obtained with the three heaters at different velocities and orientations.

EXPERIMENTAL APPARATUS

A detailed description of the experimental apparatus is given in Part I [26], so only a summary of the important features will be provided here. Three 10-mm-wide heaters of length 10, 30 and 110 mm were tested in a 10-mm × 5-mm rectangular channel. The heaters were flush-mounted to one of the channel walls facing a transparent Lexan cover which formed the wall opposite to the heaters. Figure 2 illustrates a cross-section of the channel and the heaters. All of the tests were performed with Fluorinert FC-72 at 1.36 bar (20 psia) and 4°C subcooling. Only one of the heaters was operated during a given test so that the heaters did not influence one another. Still pictures were taken with a 35-mm Nikon camera with a 1/64 000 s flash while high speed video images were obtained with a Kodak EktaPro 1000 motion analyzer. Vertical upflow was designated with the 0° reference angle and horizontal flow (with liquid flow above the heaters) with the 90° angle.

CHF MODEL

In this section, the physical mechanisms causing the vapor wave growth as measured in Part I [26] are incorporated in the development of the CHF model. The model requires knowledge of local liquid and vapor conditions which are determined using a separated two-phase model. The model is verified by comparing its predictions to CHF data for the three heaters.

Separated flow model

The hydrodynamics of the channel were theoretically modeled by solving the mass and momentum conservation equations using separated two-phase flow assumptions. At heat fluxes nearing CHF, visual observations of the two-phase mixture confirmed the flow was in fact separated over the entire length of the 10- and 30-mm heaters and over the entire 110-mm heater for most of the tests. During low velocity tests with the 110-mm heater, flow changed from separated to churn-turbulent on the downstream half of the heater at all orientations.

The separated flow model, the equations for which are detailed in Appendix A, was solved in a step-wise manner starting at the most upstream edge of the respective heater and marching downstream. Since the thickness of the vapor layer is unknown, the solution procedure required an iterative scheme for closure. The time-averaged vapor layer thickness, δ, was increased at each stream-wise step until the pressure drop across the vapor layer equaled the pressure drop across the entire channel cross section.

Figure 3(a)–(c) shows predictions of the separated flow model for each of the heaters at $U = 25$ and 200 cm s^{-1} in vertical upflow and $U = 25$ cm s^{-1} in horizontal flow, respectively. The measured CHF was used as the surface heat flux for each case for illustrative purposes. The vapor velocity is observed to increase rapidly along the length of the heater while the liquid velocity increases at a much slower rate. The velocity difference between the phases is also shown because of its strong influence on interfacial instability. Even at $U = 25$ cm s^{-1}, the vapor velocity rapidly assumes large values on all three heaters because of stream-wise evaporation and the drastic difference in density between liquid and vapor. Figure 3(a) and (b) shows increases in velocity yield a thinner vapor layer and a larger pressure drop. Comparing Fig. 3(a) and (c) reveals, at a low velocity of 25 cm s^{-1}, increasing the angle of orientation from 0 to 90° allows the vapor to occupy a larger fraction of the channel cross

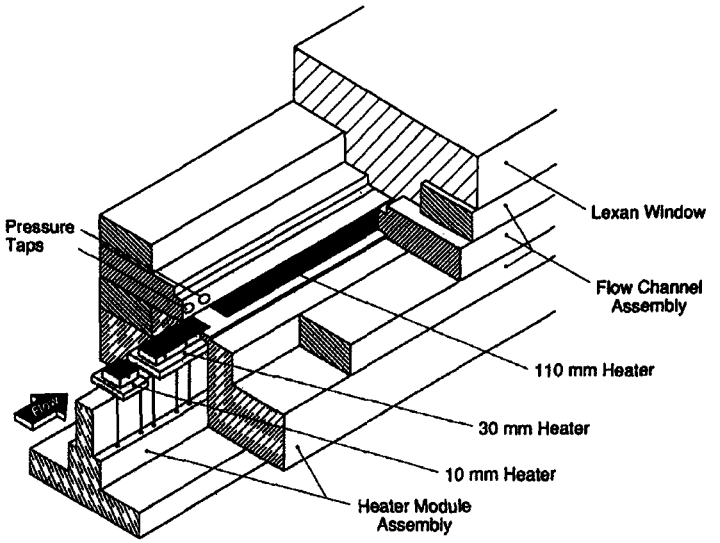

Fig. 2. Test section construction illustrating the placement of the 10-, 30- and 110-mm heaters.

section; at high inlet liquid velocities the effect of orientation on vapor layer thicknesses is negligible.

Vapor layer instability

Figure 4 shows a sinusoidal vapor–liquid interface in the confines of a flow channel. This wavy interface is an idealized representation of the waves photographed in the present study. Assuming inviscid, irrotational and two-dimensional flow, the stability of a liquid–vapor interface can be determined from classical interfacial instability theory [27, 28] once the local liquid and vapor velocities are known, hence the need for the separated flow model. Given a sinusoidal disturbance of the form $\eta(z,t) = \eta_0 e^{ik(z-ct)}$, the pressure rise across the interface can be expressed as

$$P_f - P_g = -\eta k[\rho_f''(c-U_f)^2 + \rho_g''(U_g-c)^2] - (\rho_f-\rho_g)g_n\eta \quad (4)$$

where $\rho_f'' = \rho_f \coth(kH_f)$ and $\rho_g'' = \rho_g \coth(kH_g)$. Equating pressure and surface tension forces on the interface gives the following quadratic expression for interfacial velocity:

$$\rho_g''(U_g-c)^2 + \rho_f''(c-U_f)^2 + (\rho_f-\rho_g)\frac{g_n}{k} - \sigma k = 0. \quad (5)$$

Solving equation (5) yields the following expression for c:

$$c = \frac{\rho_g''U_g + \rho_f''U_f}{(\rho_g''+\rho_f'')} \pm \sqrt{\left[\frac{\sigma k}{(\rho_g''+\rho_f'')} - \frac{g_n(\rho_f-\rho_g)}{k(\rho_g''+\rho_f'')} - \frac{\rho_g''\rho_f''(U_g-U_f)^2}{(\rho_g''+\rho_f'')^2}\right]}. \quad (6)$$

The stability of the interface depends entirely on the argument of the radical in equation (6). The first term accounts for surface tension effects and is always stabilizing. Depending on the orientation of the interface with respect to gravity, the second term can be either stabilizing or destabilizing. The third term of the argument results from the velocity difference between the liquid and vapor and is always destabilizing. When the argument is positive, c is a real number and the interface is stable. Neutral stability occurs when the argument is equal to zero. If the argument is negative, c will contain real and imaginary components, c_r and c_i, respectively, where

$$c_r = \frac{\rho_g''U_g + \rho_f''U_f}{(\rho_g''+\rho_f'')} \quad (7)$$

and

$$c_i = \sqrt{\left[\frac{\rho_g''\rho_f''(U_g-U_f)^2}{(\rho_g''+\rho_f'')^2} + \frac{g_n(\rho_f-\rho_g)}{k(\rho_g''+\rho_f'')} - \frac{\sigma k}{(\rho_g''+\rho_f'')}\right]}. \quad (8)$$

For a complex c, the interface can be expressed as

$$\eta = \mathrm{Re}\{\eta_0 e^{ik(z-ct)}\} = \eta_0 e^{kc_i t}\cos[k(z-c_r t)]. \quad (9)$$

If c_i is positive, the interface will always be unstable.

The critical wavelength is defined as the wavelength that produces a neutrally stable wave. This wavelength can be calculated by setting c_i, equation (8), equal to zero and solving for k.

$$k_c = \frac{\rho_f''\rho_g''(U_g-U_f)^2}{2\sigma(\rho_f''+\rho_g'')} + \sqrt{\left[\left(\frac{\rho_f''\rho_g''(U_g-U_f)^2}{2\sigma(\rho_f''+\rho_g'')}\right)^2 + \frac{g_n(\rho_f-\rho_g)}{\sigma}\right]}. \quad (10)$$

As the velocity difference increases, the interface rapidly becomes unstable at lower wavelengths, highlighting the failure of surface tension forces to over-

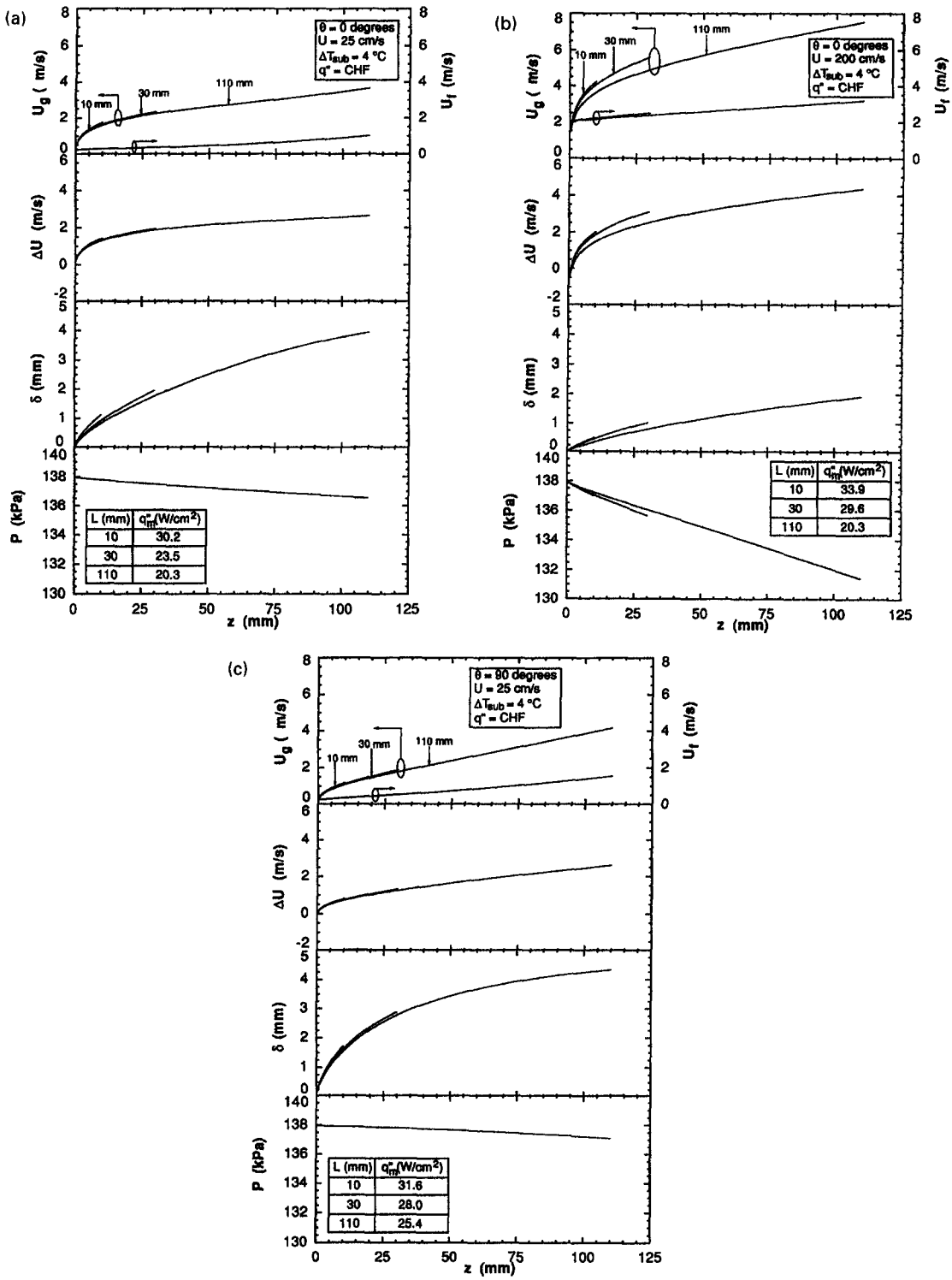

Fig. 3. Separated flow model predictions of phase velocities, vapor layer thickness, and pressure drop for (a) $U = 25$ cm s^{-1} in vertical upflow, (b) $U = 200$ cm s^{-1} in vertical upflow and (c) $U = 25$ cm s^{-1} in horizontal flow.

come the large destabilizing effect of the velocity difference. Unfortunately, calculating k_c using equation (10) involves an iteration because the hyperbolic cotangent terms in ρ_f'' and ρ_g'' also contain λ_c.

Interfacial features on the heater surface

Photographs of the heater at CHF− revealed the formation of a wavy vapor layer on the surface, with wetting occurring at the wave troughs. The distance

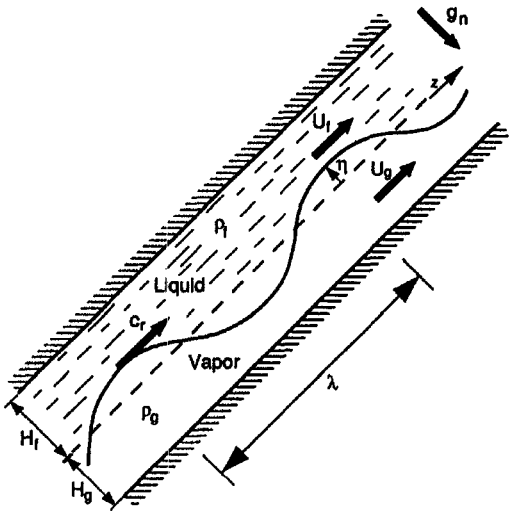

Fig. 4. Confined two-dimensional wavy liquid–vapor interface.

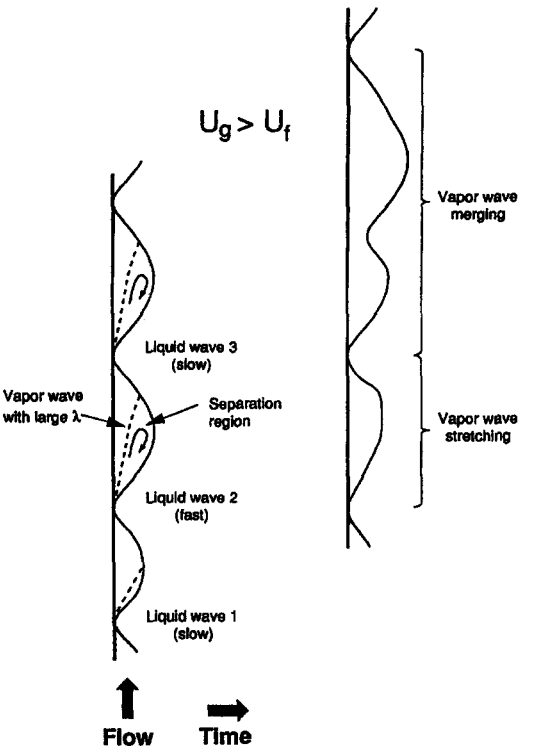

Fig. 5. Sequence of wave stretching and merging.

between wetting fronts was observed to grow in the stream-wise direction, decreasing the number of wetting fronts available for liquid replenishment on the downstream portion of the heater. The vapor layer was initiated on the first few millimeters of the heater with a wavelength equal to the Kelvin–Helmholtz critical wavelength based on local hydrodynamic conditions. On the 10-mm heater and the first 20 mm of the longer heaters, the interfacial wavelength immediately increased to $2\lambda_c$ as suggested by Galloway and Mudawar [22] who found wavelengths equal to $2\lambda_c$ at a distance of 8 mm down their 12.7-mm long heater.

Within the following 30 mm, the interfacial wavelength continued to increase, predominately because of wave stretching and merging of adjacent vapor waves. Wave merging eventually produced longer waves which assumed a constant asymptotic value midway along the 110-mm heater.

Mudawar [29] investigated the wave merging phenomenon with a thin liquid film driven by air flow. The shapes of the interfacial waves were photographed and duplicated into solid waves which facilitated measurement of drag forces on the waves and flow separation downstream of each wave. Large waves encountered larger drag forces and produced a relatively large separation region. So, when two adjacent interfacial liquid waves came close enough to one another that the downstream wave was well within the separation region of the upstream wave, the drag force on the downstream wave diminished significantly, resulting in a slowing of the downstream wave. This enabled the upstream wave to catch up and merge with the downstream wave. Interestingly, the notion of merging of fast moving waves with slower ones causing loss of smaller wavelengths has been suggested as far back as 1925 by Jeffreys [30] in his description of wind generated water waves.

The process of stretching and wave merging for the conditions of the present study is illustrated in Fig. 5. As the wavy vapor layer travels down the heater, a corresponding wavy liquid layer is formed where the troughs of the vapor waves are the peaks of the liquid waves. Since the vapor acquires a higher velocity than the liquid, the liquid waves experience drag (pressure) forces on their upstream sides. When the amplitude of the liquid wave is large enough, a separation region is established on the sheltered side of the wave. Depending upon its size, the separation region may shield part of the downstream liquid wave from the rapidly moving vapor. As a result, the sheltered wave possesses a lower stream-wise velocity than an unsheltered wave of the same amplitude. Many researchers have observed that waves with higher stream-wise velocities overtake and merge with waves with lower velocities [31–34]. In the present study, merging was observed to take place predominantly in the L_2 zone, Fig. 10 from Part I of this study [26]. As shown in Fig. 5, as two waves merge, the faster liquid wave overtakes the slower liquid wave causing both stretching in the upstream vapor wave and merging of the two downstream vapor waves.

Since in the present study waves grew on the 30- and 110-mm heaters, there were fewer wetting fronts touching the heater surface than equation (1) would predict. Based on visual observation of the wavy vapor layer, three zones were found to exist on the heaters as shown in Fig. 10 of Part I of this study. The first zone, L_1, contains the upstream of the heater where waves with lengths twice λ_c were generated. The

second zone, L_2, is predominately characterized by waves stretching and merging together because of differences in drag forces. The final zone, L_3, accounts for the balance of the heater where the waves assumed a constant asymptotic wavelength. By simply dividing the heater into the three zones and partitioning each zone into wavelengths, a ratio of the wetting fronts from a heater with wave merging to the wetting fronts without merging can be determined. For example, the ratio of wetting fronts for a heater with $L_1 < L < (L_1+L_2)$ to a heater with $z^* < L < L_1$ is equal to

$$\frac{\dfrac{L_1}{2\lambda_c}+\dfrac{L-L_1}{3\lambda_c}}{\dfrac{L}{2\lambda_c}}=\frac{L_1}{L}+\frac{2(L-L_1)}{3L}.$$

In general, this ratio can be expressed as

$$\frac{N_{\text{actual}}}{N_{2\lambda_c}}=f(L)=\begin{cases}1 & z^* < L \leqslant L_1\\ \dfrac{L_1}{L}+\dfrac{2(L-L_1)}{3L} & L_1 < L \leqslant (L_1+L_2)\\ \dfrac{L_1}{L}+\dfrac{2L_2}{3L}+\dfrac{L-(L_1+L_2)}{2L} & (L_1+L_2) < L\end{cases} \tag{11}$$

where L_1 and L_2 were observed to be approximately 20 mm and 30 mm in length, respectively. It is the existence of the second and third zones that differentiates CHF on long heaters from values predicted by the original Galloway and Mudawar [23] model based on $N_{2\lambda_c}$.

The effect of wavelength growth can also be manifested by plotting the frequency of wetting front arrival at different parts of the heater surface. Figure 6 shows this frequency as a ratio of the wave speed, c_r, calculated locally for each position, divided by the wavelength measured at the same position. The upstream zone, L_1, displays a sharp reduction in frequency due to the waves rapidly doubling their wavelength from λ_c to $2\lambda_c$. The reduction in frequency becomes less severe in the L_2 zone while in the L_3 zone frequencies seem to converge to a constant asymptotic value for each inlet velocity. Whalley [35] reported a similar asymptotic behavior has been observed for interfacial waves in annular two-phase flow.

Figure 6 can partially explain the trends indicated in Fig. 10 of Part I of this study concerning the effect of heater length on CHF. A shorter heater would encounter wetting fronts with a relatively high frequency, resulting in a high CHF. Longer heaters, on the other hand, suffer a great reduction in the frequency of wetting fronts over the downstream portions of their surfaces. This increases the downstream surface temperature at CHF− and decreases CHF. Hall Taylor and Nedderman [34] observed a similar decay of interfacial wave frequency with increasing

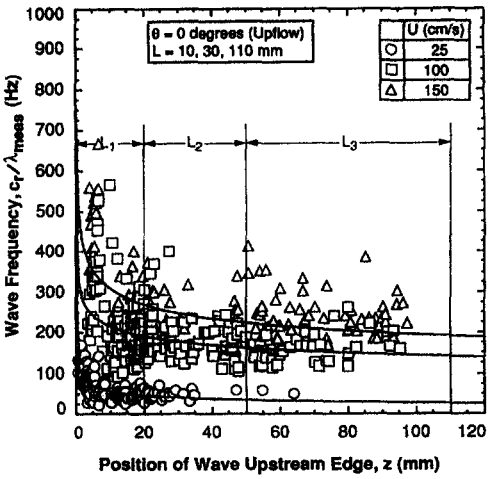

Fig. 6. Measured frequency of interfacial waves for inlet liquid velocities of 25, 100 and 150 cm s^{-1} in vertical upflow.

distance in their study of water waves in annular upflow. Initially wave coalescence sharply decreased interfacial wave frequency. Farther downstream, the distance between waves reached a quasi-steady value, causing the wave frequency in that region to approach an asymptotic value. Their results indicate that in three downstream regions, the preferred separation distances between wave peaks were integral multiples (2, 3 and 4 times) of the initial wave separation. Increases in liquid flow rate decreased the number of waves observed at the higher separation distances but did not influence the preferred separation values.

Surface energy balance and lift off heat flux

Lifting of the *most upstream wetting front* was found in Part I of this study to be the trigger mechanism that initiated CHF. Therefore the lift-off heat flux devised by Galloway and Mudawar [23] would apply to all of the present tests, but there would be fewer wetting fronts on the surface at CHF than predicted by equation (1). Introducing the ratio of wetting fronts, $f(L)$, into equations (2) and (3) yields an equation for CHF on long heaters:

$$q''_m = 0.25\rho_g h_{fg} f(L)\left(1-\frac{\lambda_c}{16(L-z^*)}\right)\left(1+\frac{c_{pf}\Delta T_{sub}}{h_{fg}}\right)\times\left[\frac{(\overline{P_f-P_g})_{\lambda=2\lambda_c}}{\rho_g}\right]^{1/2}=f(L)q''_{m,\lambda=2\lambda_c} \tag{12}$$

where $f(L)$ is defined in equation (11). It is important to note that $q''_{m,\lambda=2\lambda_c}$ in equation (12) follows exactly the form proposed by Galloway and Mudawar for vertical upflow. The effect of orientation, although not directly evident in equation (12), is implicit, though small, in the effect of g_t on U_f, U_g and δ (as predicted by the separated flow model) in λ_c and the overall effect of U_f, U_g and δ, and λ_c as well as g_n on $(\overline{P_f-P_g})_{\lambda=2\lambda_c}$ according to equation (4).

Another important implication of the asymptotic decay of wetting front frequency is the existence of an asymptotic CHF for very long heaters. There are numerous examples in the literature pointing to the existence of such an asymptote in small tubes [36, 37] and annular channels [37, 38]. Through extensive literature surveys, Tong [39] and Bergles [40] found that asymptotic CHF values do exist for long tubes in low-quality two-phase flow.

The asymptotic decay of wetting front frequency, Fig. 6, points to the existence of an asymptotic value for CHF for heaters having $(L_1+L_2)\ll L$. For these asymptotic cases,

$$\left[\frac{L_1}{L}+\frac{2L_2}{3L}+\frac{L-(L_1+L_2)}{2L}\right]\approx\frac{1}{2}$$

so equation (12) reduces to

$$q''_m = 0.125\rho_g h_{fg}\left(1+\frac{c_{pf}\Delta T_{sub}}{h_{fg}}\right)\times\left[\frac{(\overline{P_f-P_g})_{\lambda=2\lambda_c}}{\rho_g}\right]^{1/2}. \quad (13)$$

Solution procedure

Predicting CHF involves an iterative scheme consisting of, first, assigning an estimated value for CHF and using the separated flow model to calculate the local phase velocities, U_f and U_g, and vapor layer thickness, δ. These values were then utilized in the instability model to calculate z^* and λ_c. Finally, equation (12) was employed to calculate CHF. This CHF value became the input for the separated flow model in the next iteration. The procedure was stopped once the difference in the CHF values between consecutive iterations was below 0.1 W cm^{-2}.

Comparison of measured and predicted CHF

The major modification to the Galloway and Mudawar [23] CHF model was accounting for the effect of heater length on vapor wave growth. The increase in the distance between wetting fronts caused the number of wetting fronts to decrease; however, lifting of the upstream wetting front, identified by Galloway and Mudawar as the trigger mechanism for CHF on short heaters, was found to precipitate CHF on the longer heaters as well.

The predicted and measured CHF values for all of the tests are compared in Fig. 7 which shows the data falling within an error band of ±30%; the overall mean absolute error of the model predictions was 14.6%. The model predicted the data with a mean absolute error of 12.6, 13.6, and 17.5% for the 0°, 45° and 90° orientations, respectively. As the channel was rotated away from the vertical position, gravitational forces normal to the heater surface increased the force necessary to lift the wetting front from the heater. At most inlet velocities, gravitational forces were negligible as compared to inertial forces, but, at $U = 25$ cm s^{-1} and horizontal flow, gravitational forces were approximately five times greater than the inertial forces. This caused an increase in the lift-off heat flux and, hence, the predicted CHF. As inlet velocity increased, the inertial forces increased and both the vapor layer thickness and λ_c decreased, causing a decrease in the curvature of the most upstream wetting front and a decrease of the lift-off heat flux.

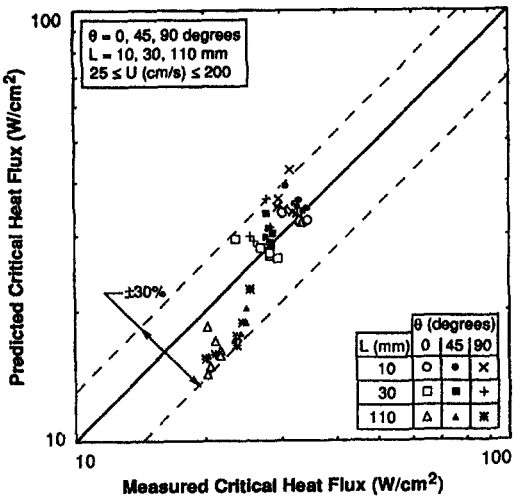

Fig. 7. Comparison of predicted and measured critical heat flux values for all heater lengths, inlet velocities and orientations.

The model predicted CHF from the 10- and 30-mm heaters, at all velocities and orientations, with mean absolute errors of 10.4 and 9.8%, respectively, but was only able to predict CHF within 23.5% for the 110-mm heater. This suggests that care should be exercised when applying this model to situations when the wavy vapor layer is able to contact the opposing wall or in the case of pipe flow, when the vapor layer extends throughout the radius.

CONCLUSIONS

A flow boiling CHF model that accounts for heater length and orientation effects was formulated. Critical heat flux values measured for 10-, 30- and 110-mm long heaters in vertical upflow, 45-degree inclined flow, and horizontal flow were utilized to verify the model. The main conclusions of the study are as follows.

(1) The spacing between consecutive wetting fronts, identified by Galloway and Mudawar as having the greatest impact on the CHF value, was observed to increase along the 30- and 110-mm heaters of the present study. Adjusting the original model to account for this wave growth allowed the model to predict the CHF data in vertical upflow with a mean absolute error of 12.6%.

(2) The present model points to the existence of an

asymptotic CHF for very long heaters as evidenced from numerous articles in the heat transfer literature.

(3) The revised model also accounts for effects of orientation in the 0–90° range, although this effect was found to be insignificant for all velocities exceeding 25 cm s^{-1}. The model predicts the CHF data for the 45° and 90° orientations with mean absolute errors of 13.6 and 17.5%, respectively.

Acknowledgements— The authors gratefully acknowledge the support of the Office of Basic Energy Sciences of the U.S. Department of Energy (Grant No. DE-FE02-93ER14394). The authors also thank the Industrial Chemical Products Division of 3M Company for donating the Fluorinert FC-72 for the present study.

REFERENCES

1. L. S. Tong and G. F. Hewitt, Overall viewpoint of flow boiling CHF mechanisms, ASME Paper 72-HT-54 (1972).
2. V. Marinelli, Critical heat flux: a review of recent publications, *Nucl. Technol.* **34,** 135–171 (1977).
3. G. F. Hewitt, Critical heat flux in flow boiling, *Heat Transfer* 1978: *Proceedings of the 6th International Heat Transfer Conference*, Toronto, Vol. 6, pp. 143–171 (1978).
4. Y. Katto, Critical heat flux in forced convective flow, *Proceedings of the ASME/JSME Thermal Engineering Joint Conference*, Honolulu, HI, Vol. 3(1), pp. 1–10 (1983).
5. S. S. Kutateladze and A. I. Leont'ev, Some applications of the asymptotic theory of the turbulent boundary layer, *Heat Transfer* 1966 *Conference*: *Proceedings of the Third International Heat Transfer Conference*, Chicago, IL, Vol. 3, pp. 1–6 (1966).
6. L. S. Tong, Boundary-layer analysis of the flow boiling crisis, *Int. J. Heat Mass Transfer* **11,** 1208–1211 (1968).
7. L. S. Tong, A phenomenological study of critical heat flux, ASME Paper 75-HT-68 (1975).
8. J. H. Lienhard and R. Eichhorn, Peak boiling heat flux on cylinders in a cross flow, *Int. J. Heat Mass Transfer* **19,** 1135–1142 (1976).
9. J. H. Lienhard and M. M. Hasan, On predicting boiling burnout with the mechanical energy stability criterion, *J. Heat Transfer Trans. ASME* **101,** 276–279 (1979).
10. G. J. Kirby, R. Staniforth and J. H. Kinneir, A visual study of forced convection boiling—Part 2. Flow patterns and burnout for a round test section, Report AEEW-R 506, United Kingdom Atomic Energy Authority Reactor Group (1967).
11. W. Hebel, W. Detavernier and M. Decreton, A contribution to the hydrodynamics of boiling crisis in a forced flow of water, *Nucl. Engng Des.* **64,** 433–445 (1981).
12. J. Weisman and B. S. Pei, Prediction of critical heat flux in flow boiling at low qualities, *Int. J. Heat Mass Transfer* **26,** 1463–1477 (1983).
13. M. P. Fiori and A. E. Bergles, Model of critical heat flux in subcooled flow boiling, *Heat Transfer* 1970: *Proceedings of the Fourth International Heat Transfer Conference*, paper B6.3. Paris (1970).
14. S. B. Van der Molen and F. W. B. M. Galjee, The boiling mechanism during burnout phenomena in subcooled two-phase water flows, *Heat Transfer* 1978: *Proceedings of the Sixth International Heat Transfer Conference*, Toronto, Vol. 1, pp. 381–385 (1978).
15. Y. Haramura and Y. Katto, A new hydrodynamic model of critical heat flux, applicable widely to both pool and forced convection boiling on submerged bodies in saturated liquids, *Int. J. Heat Mass Transfer* **26,** 389–399 (1983).
16. R. Hino and T. Ueda, Studies on heat transfer and flow characteristics in subcooled flow boiling—Part 2. Flow characteristics, *Int. J. Multiphase Flow* **11,** 283–297 (1985b).
17. I. Mudawar, T. A. Incropera and F. P. Incropera, Boiling heat transfer and critical heat flux in liquid films falling on vertically-mounted heat sources, *Int. J. Heat Mass Transfer* **30,** 2083–2095 (1987).
18. C. H. Lee and I. Mudawar, A mechanistic critical heat flux model for subcooled flow boiling based on local bulk flow conditions, *Int. J. Multiphase Flow* **14,** 711–728 (1988).
19. I. Mudawar and D. E. Maddox, Critical heat flux in subcooled flow boiling of fluorocarbon liquid on a simulated electronic chip in a vertical rectangular channel, *Int. J. Heat Mass Transfer* **32,** 379–394 (1989).
20. Y. Katto, A physical approach to critical heat flux of subcooled flow boiling in round tubes, *Int. J. Heat Mass Transfer* **33,** 611–620 (1990).
21. Y. Katto, Prediction of critical heat flux of subcooled flow boiling in round tubes, *Int. J. Heat Mass Transfer* **33,** 1921–1928 (1990).
22. J. E. Galloway and I. Mudawar, CHF mechanism in flow boiling from a short heated wall—I. Examination of near-wall conditions with the aid of photomicrography and high-speed video imaging, *Int. J. Heat Mass Transfer* **36,** 2511–2526 (1993).
23. J. E. Galloway and I. Mudawar, CHF mechanism in flow boiling from a short heated wall—II. Theoretical CHF model, *Int. J. Heat Mass Transfer* **36,** 2527–2540 (1993).
24. J. E. Galloway and I. Mudawar, A mechanistic view of the CHF enhancement effect attributed to flow curvature, *ANS Proceedings*: 1993 *National Heat Transfer Conference*, Atlanta, GA, Vol. HTC-Vol. 7, pp. 9–21 (1993).
25. J. H. Lienhard, Things we don't know about boiling heat transfer: 1988, *Int. Commun. Heat Mass Transfer* **15,** 401–428 (1988).
26. C. O. Gersey and I. Mudawar, Effects of heater length and orientation on the trigger mechanism for near-saturated flow boiling critical heat flux—I. Photographic study and statistical characterization of the near-wall interfacial features, *Int. J. Heat Mass Transfer* **38,** 629–641 (1995).
27. H. Lamb, *Hydrodynamics*. Dover New York (1945).
28. L. M. Milne-Thomson, *Theoretical Hydrodynamics*. Macmillan, New York (1960).
29. I. Mudawar, Interfacial instabilities of air-driven liquid films, *Int. Commun. Heat Mass Transfer* **13,** 535–543 (1986).
30. H. Jeffreys, On the formation of water waves by wind, *Proc. R. Soc. Lond. Ser. A* **107,** 189–206 (1925).
31. N. Andritsos and T. J. Hanratty, Interfacial instabilities for horizontal gas–liquid flows in pipelines, *Int. J. Multiphase Flow* **13,** 583–603 (1987).
32. A. S. Telles and A. E. Dukler, Statistical characteristics of thin, vertical, wavy, liquid films, *I & EC Fundam.* **9,** 412–421 (1970).
33. N. S. Hall Taylor, G. F. Hewitt and P. M. C. Lacey, The motion and frequency of large disturbance waves in annular two-phase flow of air–water mixtures, *Chem. Engng Sci.* **18,** 537–552 (1963).
34. N. S. Hall Taylor and R. M. Nedderman, The coalescence of disturbance waves in annular two phase flow, *Chem. Engng Sci.* **23,** 551–564 (1968).
35. P. B. Whalley, *Boiling, Condensation, and Gas–Liquid Flow*. Clarendon Press, Oxford (1987).
36. A. E. Bergles, Subcooled burnout in tubes of small diameter, ASME Paper 63-WA-182 (1963).
37. A. P. Ornatskiy, The effect of basic regime parameters

and channel geometry on critical heat fluxes in forced convection of subcooled water, *Heat Transfer—Sov. Res.* **1**, 17–22 (1969).
38. V. I. Tolubinsky, A. K. Litoshenko and V. L. Shevtsov, Heat transfer crisis at water boiling in annular channels with external and internal heating, *Heat Transfer* 1970: *Proceedings of the Fourth International Heat Transfer Conference*, Paris, Vol. 6, paper B 6.11 (1970).
39. L. S. Tong, Boiling crisis and critical heat flux, TID-25887, U.S. Atomic Energy Commission (1972).
40. A. E. Bergles, Burnout in boiling heat transfer—II. Subcooled and low quality forced-convection systems, *Nucl. Saf.* **18**, 154–167 (1977).
41. G. B. Wallis, Annular two-phase flow—Part 1. A simple theory, *J. Basic Engng* **92**, 59–72 (1970).
42. J. C. Dallman, Investigation of separated flow model in annular gas-liquid two-phase flows, Ph.D. Dissertation, University of Illinois, Urbana–Champaign (1978).
43. J. M. Kaufman, Post critical heat flux heat transfer to water in a vertical tube, M.Sc. Thesis, MIT, Boston, MA (1976).

APPENDIX A—SEPARATED FLOW MODEL

Phase velocities

$$U_g = \frac{q''z}{\rho_g \delta (c_{pf}\Delta T_{sub} + h_{fg})} \tag{A1}$$

$$U_f = \frac{\rho_f UHw - \rho_g U_g \delta w}{\rho_f (H-\delta)w} = \frac{U}{\left(1-\frac{\delta}{H}\right)} - \frac{q''z}{\rho_f (H-\delta)(c_{pf}\Delta T_{sub} + h_{fg})}. \tag{A2}$$

Pressure drop

$$-\frac{dP}{dz} = \frac{1}{\delta}\frac{d}{dz}(\rho_g \delta U_g^2) + \frac{1}{\delta}\tau_i + \left(\frac{1}{\delta}+\frac{2}{w}\right)\tau_g + \rho_g g_t = -\left(\frac{dP}{dz}\right)_A - \left(\frac{dP}{dz}\right)_F - \left(\frac{dP}{dz}\right)_G \tag{A3}$$

$$-\left(\frac{dP}{dz}\right)_A = \frac{d}{dz}\left[\rho_f U_f^2\left(1-\frac{\delta}{H}\right) + \rho_g U_g^2 \frac{\delta}{H}\right] \tag{A4}$$

$$-\left(\frac{dP}{dz}\right)_F = \left(\frac{1}{H} + \frac{2(H-\delta)}{wH}\right)\tau_f + \left(\frac{1}{H}+\frac{2\delta}{wH}\right)\tau_g \tag{A5}$$

$$-\left(\frac{dP}{dz}\right)_G = \left[\rho_f\left(1-\frac{\delta}{H}\right) + \rho_g \frac{\delta}{H}\right] g_t. \tag{A6}$$

Wall shear stress

$$\tau_k = \frac{1}{2} f_k \rho_k U_k^2 = \frac{1}{2}\left[0.0791\left[\frac{\rho_k U_k D_{h,k}}{\mu_k}\right]^{-0.25}\right]\rho_k U_k^2. \tag{A7}$$

Determination of interfacial shear stress

Several researchers have correlated the interfacial friction factor for various separated two-phase flows: Wallis [41], Dallman [42] and Whalley [35] for annular flow and Kaufman [43] for inverted annular pipe flow. Kaufman [43] substituted the vapor layer thickness for the liquid core thickness in utilizing the interfacial friction factor relation originally developed by Wallis. In order to account for intermittent contact of the interface with the wall and the changing vapor layer thickness, Galloway and Mudawar [23] assumed a constant value of 0.5 for the interfacial friction factor.

Using the Wallis model, the interfacial friction factor increases from 0.1 at $\delta = 0.5$ mm to 1.0 at $\delta = 4.5$ mm while the interfacial friction factors predicted by the Kaufman and Dallman models decrease from about 1.5 at $\delta = 0.5$ mm to 0.2 at $\delta = 4.5$ mm. For the present analysis, the interfacial friction factor was varied between 0.2 and 1.0, and the total pressure drop changed by less than ±16.5% across the 110-mm heater. This suggests assuming a constant average interfacial friction factor in the range predicted from the above models would yield satisfactory results. Like Galloway and Mudawar's, the present apparatus featured a growing vapor layer that periodically touched the heater surface; thus, a constant friction factor of 0.5, as recommended by Galloway and Mudawar, was utilized for all the separated model predictions of the present study.

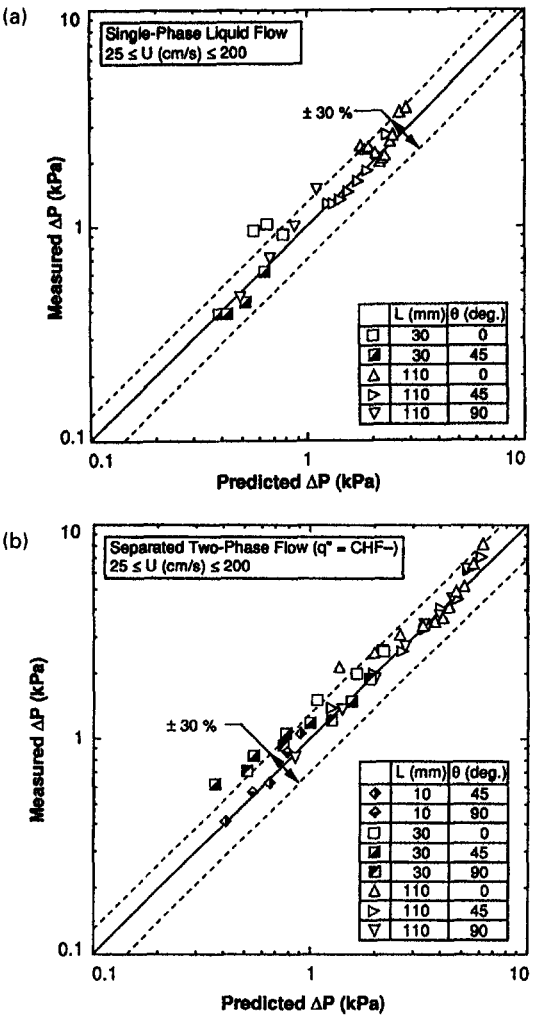

Fig. A1. Comparison of measured and predicted pressure drop for (a) single-phase liquid flow with the predictions based on the Blasius equation and (b) conditions nearing critical heat flux with predictions based on the separated flow model.

Comparison of separated flow model predictions to experimental data

A high accuracy (±1 psi) differential pressure transducer was used to measure the pressure drop across each of the three heaters. In order to validate the use of the Blasius friction factor with the present channel design, pressure drops predicted for single-phase liquid flow across the 110-mm heater (all three orientations) and 30-mm heater (0° and 45° orientations) were compared to the measured values; the single-phase frictional pressure drops across the 10-mm

heater and the 30-mm heater in horizontal flow were too small to be accurately measured even with the high accuracy pressure transducer. Figure A1(a) shows most of the single-phase pressure drop data for the 30- and 110-mm heaters are within a $\pm 30\%$ error band, illustrating the Blasius correlation is a reasonable choice for wall shear stress calculations.

Figure A1(b) compares the predicted and measured pressure drops across the heaters just prior to CHF for many of the tests; again, the pressure drop for some of the tests was too small to be accurately measured. Almost all the data points seem to fall within a $\pm 30\%$ error band, demonstrating the validity of the separated flow model as well as the choice of interfacial friction factor. It should be re-emphasized that the separated flow model assumes a smooth vapor–liquid interface. Visually, however, the vapor layer was observed to posses a wavy interface. Further, during tests with the 110-mm heater and inlet velocities of 25 and 50 cm s^{-1}, the vapor and liquid appeared well mixed throughout the channel cross section on the downstream portion of heater. These two factors explain some of the deviations of experimental data from the model predictions.